

A finite difference code designed to study nonlinear magneto-convection and dynamo evolution

Shravan M. Hanasoge & Jonathan Pietarila Graham

*Max-Planck-Institut für Sonnensystemforschung, Max Planck Straße 2, 37191
Katlenburg-Lindau, Germany*

Abstract

The generation and maintenance of magnetic fields in turbulent plasmas is a phenomenon of interest to many areas of astrophysics. The evolution and interaction of magnetic fields with turbulent convecting plasma is described by the non-linear resistive Magneto-Hydrodynamic (MHD) equations, solutions to which may be non-trivial to extract, depending on the regime of study. In particular, a minimum requirement is the use of precise high-order spatio-temporal schemes to accomplish the computation. To estimate derivatives of various terms, we implement Fast Fourier Transforms (FFTs) along directions where periodicity may apply and sixth-order accurate compact finite differences along directions where the fluid is stratified. Temporal evolution is achieved through the application of the classical fourth-order Runge-Kutta scheme. The code is written according to the Message Passing Interface (MPI) 1.0 standard, with the domain distributed along one of the horizontal directions. We discuss the validation of the code on a number of tests; some runs with dynamos and isotropic MHD turbulence are presented as well.

Key words: Magnetohydrodynamics, Numerical simulations, Dynamo theory
PACS: 47.65.-d, 75.40.Mg, 91.25.Cw

1. Introduction

Magnetic fields play an important role in determining the dynamics and structure of plasmas. The Sun, for example, exhibits a 22 year cycle over which the large scale field reverses polarity, passing through minimum and maximum magnetic activity phases. During these phases, local changes in dynamical properties of convection, flows, and waves have been observed. Mean field dynamo action is thought by some to be the primary cause of the dispersal and regeneration of the solar magnetic fields. Close to the solar photosphere, magnetic field submergence and emergence occurs far more dynamically, on timescales of the order of several minutes [e.g 1]. These could be small-scale dynamos and may not lead to a mean field. The direct turbulent energy cascade is unidirectional with the large scales feeding the small. However, the inverse cascade, a process

by which small-scale magnetic helicity moves through wave-number space to form large-scale coherent mean fields [2, 3, 4] is known to occur in situations of MHD turbulence. It is thought that this phenomenon occurs primarily when non-zero helicity is injected into the system.

The α effect is a concept central to current theoretical models of solar and stellar dynamo action. Turbulence and magnetic buoyancy act in collusion to raise and twist strands of field, essentially transforming field initially in one direction to another. For example a mechanism proposed to explain the generation of poloidal field from an initially toroidal state, is the α effect. In fact, understanding the nature of the α effect and its dependencies on turbulent velocity correlations is quite crucial to answering the questions of whether stellar dynamos are predictable and if the concept of the α effect is pertinent and useful. Recently, [5], [6] studied a rotating, convecting dynamo in the Boussinesq limit and found that at almost all magnetic and hydrodynamic Reynolds numbers, there was small-scale dynamo action; however, they failed to observe the emergence of a mean field (such a field has now been produced in simulations [7]). Furthermore, they found that it was fairly difficult to estimate the coefficient tensor characterizing the α effect, and in fact, found that it fluctuated significantly over long times. We are interested in investigating further the questions of when and why inverse cascades arise.

In this paper, we discuss the validation of a semi-spectral code designed to study magnetized convecting plasmas and dynamos. The code was originally written to study linear wave propagation in magnetized solar environments [8, 9, 10] such as sunspots, and has now been extended to compute the fully nonlinear compressible MHD equations. Verification to confirm the convergence rates and order of accuracy have been performed in e.g. [10]. The non-linear testing performed here also strengthens the case for the pre-existing linear code. The code is tested on a number of standard validation problems, on the Archontis dynamo [11] and a free decay case of the ABC flow [e.g. 12].

2. Equations

We solve the 3D time-dependent, compressible, resistive MHD equations in conservative form [e.g. 13]:

$$\frac{\partial \rho}{\partial t} = -\nabla \cdot (\rho \mathbf{v}), \quad (1)$$

$$\frac{\partial \rho \mathbf{v}}{\partial t} = \nabla \cdot \left(-\rho \mathbf{v} \mathbf{v} + \mathbf{B} \mathbf{B} - \left[p + \frac{1}{2} |\mathbf{B}|^2 \right] \mathbf{I} \right) + \rho \mathbf{g} + \rho \mathbf{F} + \nabla \cdot \mathbf{T}, \quad (2)$$

$$\begin{aligned} \frac{\partial e}{\partial t} = & -\nabla \cdot \left(\mathbf{v} \left(e + p + \frac{1}{2} |\mathbf{B}|^2 \right) - \mathbf{B} (\mathbf{v} \cdot \mathbf{B}) \right. \\ & \left. - \mathbf{B} \times \eta \nabla \times \mathbf{B} - \mathbf{v} \cdot \mathbf{T} - \kappa \nabla T \right) + \rho (\mathbf{g} \cdot \mathbf{v}) + \rho \mathbf{v} \cdot \mathbf{F}, \end{aligned} \quad (3)$$

$$\frac{\partial \mathbf{B}}{\partial t} = -\nabla \cdot (\mathbf{v} \mathbf{B} - \mathbf{B} \mathbf{v}) + \nabla \times (\eta \nabla \times \mathbf{B}), \quad (4)$$

where ρ is the density, \mathbf{v} the vector velocity, \mathbf{B} the magnetic field, \mathbf{g} , gravity (if stratified), p the pressure, T the temperature, and \mathbf{F} is an external forcing term. The identity tensor is denoted by \mathbf{I} . The magnetic permittivity constant $4\pi\mu$ has already been absorbed into the definition of the field. The coefficient of thermal conductivity is denoted by κ . Choosing the ideal gas equation of state allows us to write the energy e as:

$$e = \frac{p}{(\gamma - 1)} + \frac{1}{2}\rho|\mathbf{v}|^2 + \frac{1}{2}|\mathbf{B}|^2, \quad (5)$$

where γ is the ratio of specific heats of the gas, with the first term denoting the internal energy of the system. The magnetic resistivity is given by η . In the momentum and energy equations, the tensor $\underline{\boldsymbol{\tau}}$ is defined as:

$$\underline{\boldsymbol{\tau}}_{ij} = \mu \left(\frac{\partial u_i}{\partial x_j} + \frac{\partial u_j}{\partial x_i} - \frac{2}{3}\delta_{ij}\nabla\cdot\mathbf{v} \right), \quad (6)$$

where μ is the viscosity. All the field variables are defined numerically on the grid points. Because we use a non-staggered grid, all quantities and derivatives thereof are defined on the grid points at all times; consequently this definition applies when estimating numerical errors in the temporal evolution of variables. The conservation equations are dealt with component by vector component in the precise manner as stated in the equations. For example, when computing the tensorial divergence term in the momentum equation (2), we calculate the derivatives along each of the (x, y, z) directions and place them in the appropriate component of the momentum equation. No additional steps such as separating the upwind or downwind fluxes are incorporated nor is the divergence-free constraint on \mathbf{B} explicitly maintained.

The diffusion terms in the momentum equations are computed in a two step process: first the six independent components of the stress tensor $\underline{\boldsymbol{\tau}}$ are computed. The divergence of the tensor is estimated in the manner as before, i.e., component by component. Similarly, the diffusion term in the induction equation (4) is also computed in two steps: first $\eta\nabla\times\mathbf{B}$ and then the curl of this quantity.

We choose a series of non-stratified (i.e. $\mathbf{g} = 0$), non-thermally conducting ($\kappa = 0$) problems to study the numerical accuracy of the code. The compact finite difference [14] scheme has been tested on a number of linear problems [15, 8, 9, 10]. Here we extend the studies to tests of the non-linear MHD equations; in particular we quantify the discretization errors associated with capturing the various fluid properties. This is not a problem in an isotropic case because our default strategy is to use FFTs in all three directions when such ideal conditions prevail. However when studying turbulence in a stratified medium, we revert to using compact finite differences along the direction of stratification. To study the errors associated with using a mixed FFT-finite difference spatial combination, in addition to test cases that have analytical solutions, we compare simulations of the compressible Archontis dynamo [e.g. 11, 16] and free decay computed using these two methods.

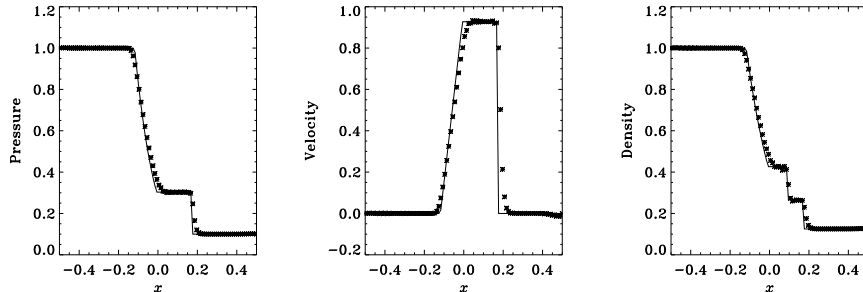


Figure 1: 1D simulation of the shock propagating in a Sod tube at $t = 0.1$; the shock is still unaffected by the boundary. Compact finite differences with non-periodic Dirichlet boundary conditions (all variables are forced to retain their initial values) are applied. The solid line is the exact solution obtained from a numerical Riemann solver while the asterisks show the computation. One hundred grid points were used in the computation.

3. Tests and Results

Sod shock tube We qualitatively study the one- and rotated three-dimensional Sod shock tube. The test involves a gas initially at rest with two regions separated by a diaphragm. At $t = 0$, the state of the gas on one side is initialized to $p = 1$, $\rho = 1$, $v = 0$ and on the other, $p = 0.1$, $\rho = 0.125$, $v = 0$. The ratio of specific heats, γ is set to 1.4. Because we are unable to model exact discontinuities, we use the following approximations ($-0.5 \leq x \leq 0.5$):

$$p = 0.1 + \frac{0.9}{1 + \exp\left[\frac{x}{0.001}\right]}, \quad (7)$$

$$\rho = 0.125 + \frac{0.875}{1 + \exp\left[\frac{x}{0.001}\right]}. \quad (8)$$

The diaphragm is then broken and a shock wave is set off. We solve this problem with the Navier-Stokes equations, i.e. $\mathbf{B} = 0$, $\mathbf{F} = 0$, with $\mu = 10^{-3}$. This small value of viscosity is required to ensure the stability of the code. The spatial and temporal resolutions were chosen to be $\Delta x = 0.01$ and $\Delta t = 0.0025$ respectively. Dirichlet boundary conditions where all variables maintain their initial values are enforced. Consequently, we have to terminate the calculation before the shocks get too close to the boundaries. A snapshot of the simulation at $t = 0.1$ is shown in Figure 1.

In order to study the effect of the combined spatial scheme, we rotate the Sod tube according to the following transformation [17]:

$$x_1 = (x \cos \beta + y \sin \beta) \cos \alpha + z \sin \alpha, \quad (9)$$

where $\sin \alpha = 2/3$ and $\sin \beta = 2/\sqrt{5}$, and $0 < x, y, z < 1$. The shock is initiated with the following pressure and density jumps:

$$p = 0.1 + \frac{0.9}{1 + \exp\left[\frac{x_1 - 0.65}{0.001}\right]}, \quad (10)$$

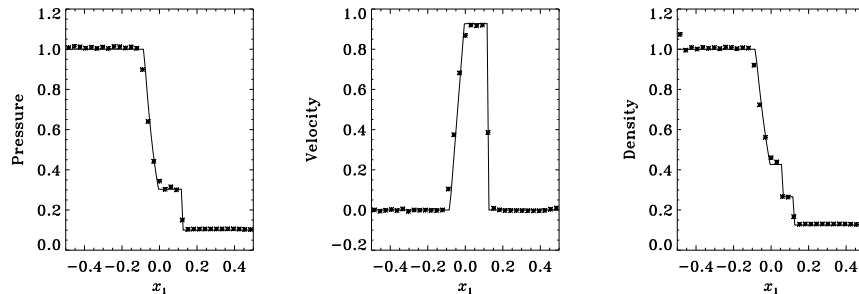


Figure 2: The Sod tube inclined at an angle to the x -axis shown at $t = 0.07$. The horizontal axis is x_1 , the coordinate along the direction of the motion of the shock. The spatial scheme is a combination of FFTs in two directions and compact finite differences along the third, with periodic boundaries. The effect of the periodic boundaries becomes very apparent at later times; an early manifestation is seen on the left boundary in the density plot. The solid line is the analytical solution while the legends show the computation.

$$\rho = 0.125 + \frac{0.875}{1 + \exp\left[\frac{x_1 - 0.65}{0.001}\right]}. \quad (11)$$

One hundred grid points to resolve each of the directions with the time step set to $\Delta t = 0.001$. A snapshot of the shock along the rotated x_1 axis at $t = 0.07$ is shown in Figure 2; for ease of viewing, the horizontal axis has been translated so as to place the shock at the center of the plot.

Brio-Wu MHD shock tube We study this co-planar MHD Riemann problem [18] in one dimension only. As in the Sod tube, the initial condition consists of two regions of plasma separated by a diaphragm, with the following properties on the left: $p = 1$, $\rho = 1$, $B_x = 0.75$, $B_y = 1$, and on the right, $p = 0.1$, $\rho = 0.125$, $B_x = 0.75$, $B_y = -1$. The ratio of the specific heats of the gas is $\gamma = 2$. A non-zero viscosity is essential in order to stabilize the calculation and damp the high wave numbers. We perform a high-resolution calculation to determine the minimum required viscosity for stability; for subsequent lower resolution calculations, we scale the viscosity according to $\mu \propto \Delta x^2 / \Delta t$. With $n_x = 800$, we find $\mu = 10^{-4}$; thus for the $n_x = 200$ case, $\mu = 10^{-3}$ is approximately the minimum value of viscosity, although some aliasing is encountered. The time step is set to $\Delta t = 10^{-5}$. Compact finite differences with zero Neumann boundary conditions were applied to resolve the spatial structure of the shocks. The results of the calculation are shown in Figure 3. We also performed simulations with $n_x = 400$, the results of which, although not shown here, match the $n_x = 800$ case far better than the $n_x = 200$ case. Primarily, it is the viscosity that alters the solutions significantly.

Circularly polarized Alfvén waves We study the 2D propagation of circularly polarized Alfvén waves in a periodic domain. These waves are solutions to the full non-linear ideal MHD equations [19]. The wave propagates at an angle $\alpha = 30^\circ$ to the horizontal axis. The horizontal edges of the box are $0 < x < 1/\cos\alpha$, $0 < y < 1/\sin\alpha$; the initial conditions are $\rho =$

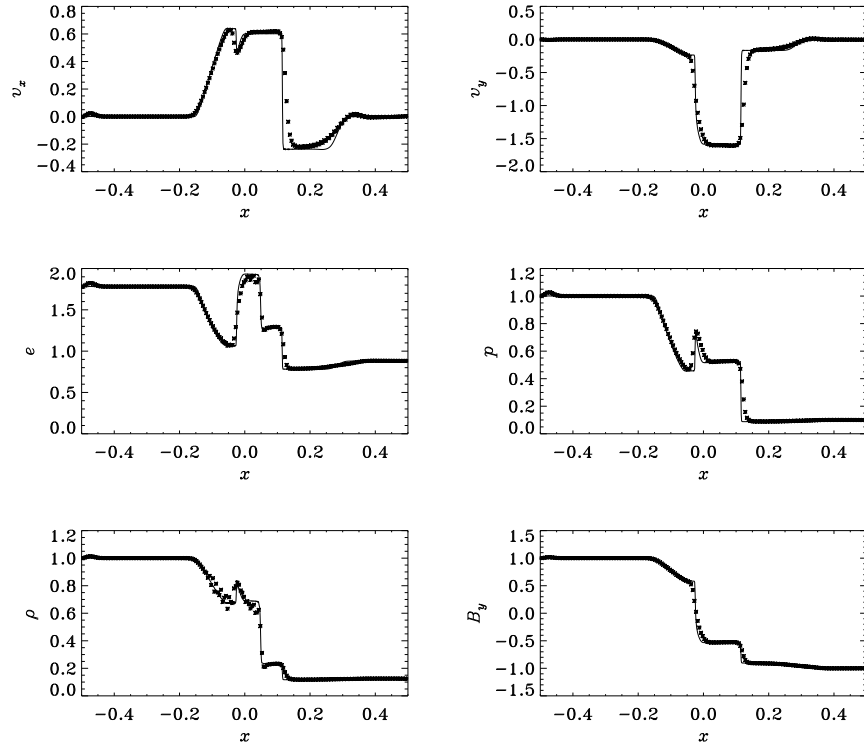


Figure 3: The Brio-Wu MHD shock tube; the two components of velocity, total energy (internal + kinetic + magnetic), pressure, density, and B_y are shown at $t = 0.08$. The solid line shows the solution for $\mu = 10^{-4}$, $n_x = 800$, and the symbols denote the solution for $\mu = 10^{-3}$, $n_x = 200$. In order to maintain convergence, the viscosity must be scaled as $\sim \Delta x^2 / \Delta t$. Compact finite differences with zero-derivative Neumann boundary conditions were applied.

1, $p = 0.1$, $\gamma = 5/3$, $B_{\parallel} = 0 = v_{\parallel}$, $B_{\perp} = 0.1 \sin(2\pi(x \cos \alpha + y \sin \alpha)) = v_{\perp}$, $B_z = 0.1 \cos(2\pi(x \cos \alpha + y \sin \alpha)) = v_z$, where the rotated axes are related to the (x, y) coordinates according to: $B_{\perp} = B_y \cos \alpha - B_x \sin \alpha$, and $B_{\parallel} = B_y \sin \alpha + B_x \cos \alpha$. As the wave propagates, the magnetic and hydrodynamic energies are constant. The wave returns to its original state at $t=1$, at which point the errors in the solution can be computed. We study this case with only FFTs - and therefore find the errors to be extremely small. The errors in the L_2 and L_{∞} norms estimated for B_x at $t = 5$ are listed in Table 3; snapshots of the wave at different instants are displayed in Figure 4.

n_x	L_2 error	L_{∞} error
8	9.11×10^{-13}	1.70×10^{-13}
16	1.62×10^{-13}	3.41×10^{-13}
32	8.71×10^{-14}	3.34×10^{-13}

Errors in B_x estimated at $t = 5$ by comparing the solution with the initial condition.

The next step is to test the combined scheme; here again, we rotate the axis of propagation in the same manner as that for the Sod tube (Eq. [9]), where α, β are as defined before, $0 \leq x < 3$, and $0 \leq y, z < 1.5$. The Alfvén wave is initialized in the $(1, 2, 3)$ coordinate system: $B_1 = 1, B_2 = 0.1 \sin(2\pi x_1) = v_2, B_3 = 0.1 \cos(2\pi x_1) = v_3, v_1 = 0$. The time step for this simulation was $\Delta t = 0.01$, and the spatial grid, of the form $(n_x, n_x/2, n_x/2)$, where $n_x = [16, 32, 64, 128]$. We perform two simulations, one with the entirely FFT based spatial scheme and the other, the combined scheme with compact finite differences along the z direction and FFTs in the two other directions. The propagation time for one full traversal is $\delta t = 1$, at which point the solution is expected to return to its initial state. Note that in these calculations, we found $|\nabla \cdot B| \lesssim 10^{-12}$. The results of these calculations are shown in Figure 5.

Shown in Figure 6 is the error related to the dispersion of the method as a function of time. We plot the L_{∞} norm of the difference $v_z(x, y, z, t) - v_z(x, y, z, t = 0)$ for the $n_x = 32, n_y = 16 = n_z$ case as a function of time; the error growth rate is seen to be linear. Note that with non-periodic or forced boundaries, e.g. [20] have discussed the existence of boundary instabilities for high-order compact-finite-difference schemes. For the cases discussed here and other linear and non-linear problems studied hitherto using the identical formulation of the compact finite differences as applied here [e.g. 15, 8, 9], such instabilities have not been seen.

3.1. Archontis dynamo

The Archontis dynamo [11] has the property that in a number of parameter regimes, it reaches the state of saturation within a few diffusion times, i.e., the magnetic and velocity fields arrive at stationary points in phase space. The interesting aspect of this dynamo is that the time derivatives of the system approach zero rapidly, allowing for the investigation of the processes involved

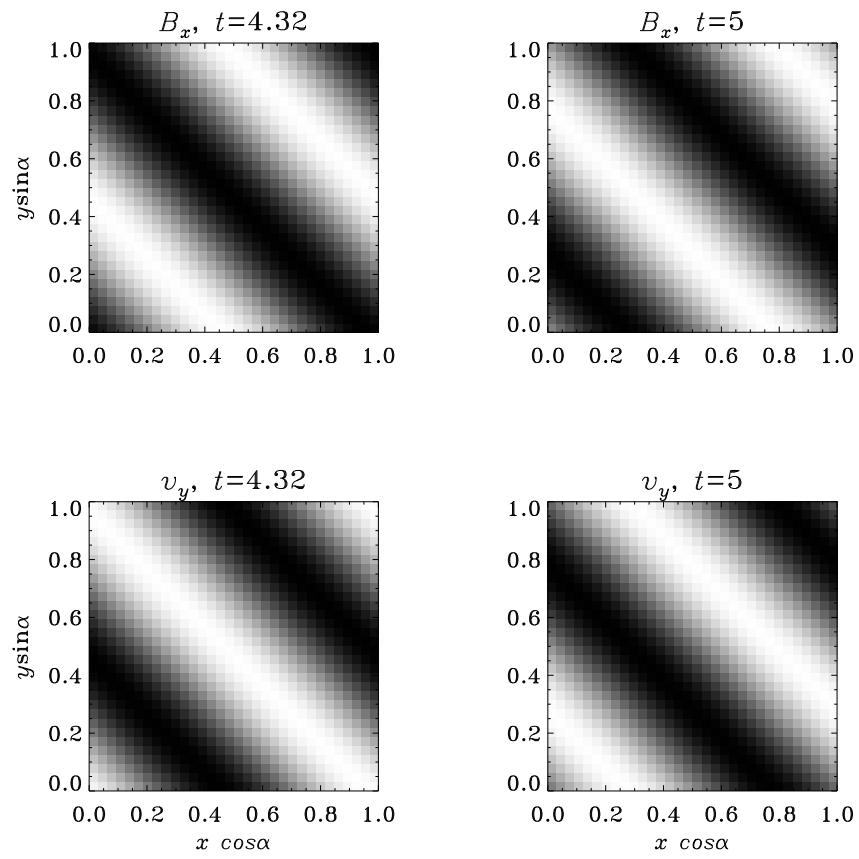


Figure 4: Snapshots of the wave at two different time instants, $t = 4.32, 5$; the upper two panels show B_x while the lower two display v_y at the same time instants.

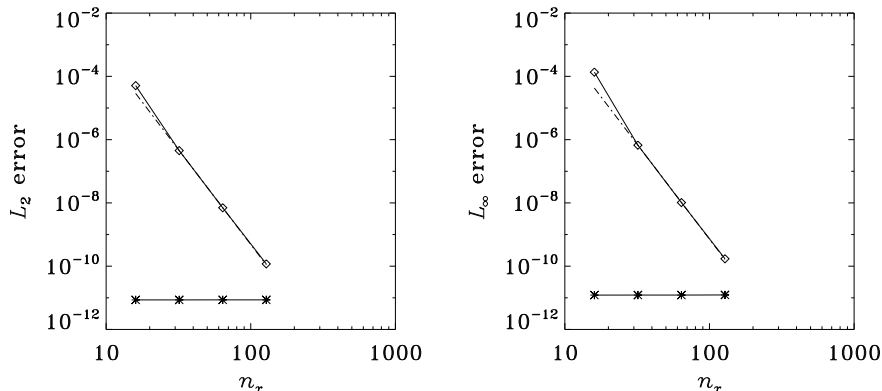


Figure 5: L_2 and L_∞ errors in v_x , defined as $\|v_x(t) - v_x(0)\|$, at $t = 2$ for the 3D case of propagating circularly polarized Alfvén waves. Two different spatial schemes were used: (1) FFTs in the three spatial directions (stars) and (2) the combined scheme (diamonds). The dot-dash line is the theoretical error drop-off for the finite differences ($\propto (\Delta x)^{-6}$). It is seen that the errors for scheme (1) are flat and do not change with increasing grid resolution. This is because the wave is fully resolved, even by the lowest resolution grid, and the all-FFT scheme, converged to the extent the time stepping will allow. The compact finite difference case is seen to rapidly converge.

in saturation. We recover a similar behaviour in our calculations as well. The compressible case was originally studied by [11] and an incompressible counterpart by [16]. We simulate the specific case discussed in [16], however, in the moderately compressible limit, with a characteristic initial state Mach number $M_0 \sim 0.39$. The initial condition is $\mathbf{v} = (\sin z, \sin x, \sin y) = \mathbf{B}$, where $0 \leq (x, y, z) < 2\pi$, $p = 4$, $\rho = 1$, $\gamma = 5/3$, and $\mu = 0.01 = \eta$. Since it is a non-stratified medium, $\mathbf{g} = 0$; however a non-zero external forcing term drives the system: the sines term $\mathbf{F}(x, y, z) = 0.01(\sin z, \sin x, \sin y)$. The forcing term acts on the momenta and indirectly, the magnetic fields, leading to increased dissipative losses, that are then channelled into the internal energy through the dissipative loss terms in the energy equation (3). Note that because we set to zero the thermal conductivity, κ , in equation (3), the temperature of the system keeps increasing in direct proportion with the internal energy, $T \propto p/(\gamma - 1)$. The time step was set at $\Delta t = 0.01$, $n_x = 96 = n_y = n_z$ and the side lengths of the box were all 2π . In order to maintain the stability of the algorithm, we apply a filter in the Fourier domain to remove the upper third of the wave number spectrum (using the FFTW real data routines):

$$\mathcal{F}(k_i) = \frac{1}{1 + \exp(2(i - 32))}, \quad (12)$$

where i lies in the range $[0, 48]$. Results from the simulations are shown in Figures 7, 8 and 9. We define the kinetic and magnetic energies as $\rho|\mathbf{v}|^2/2$ and $|\mathbf{B}|^2/2$ respectively. In both simulations, the errors in maintaining divergence-

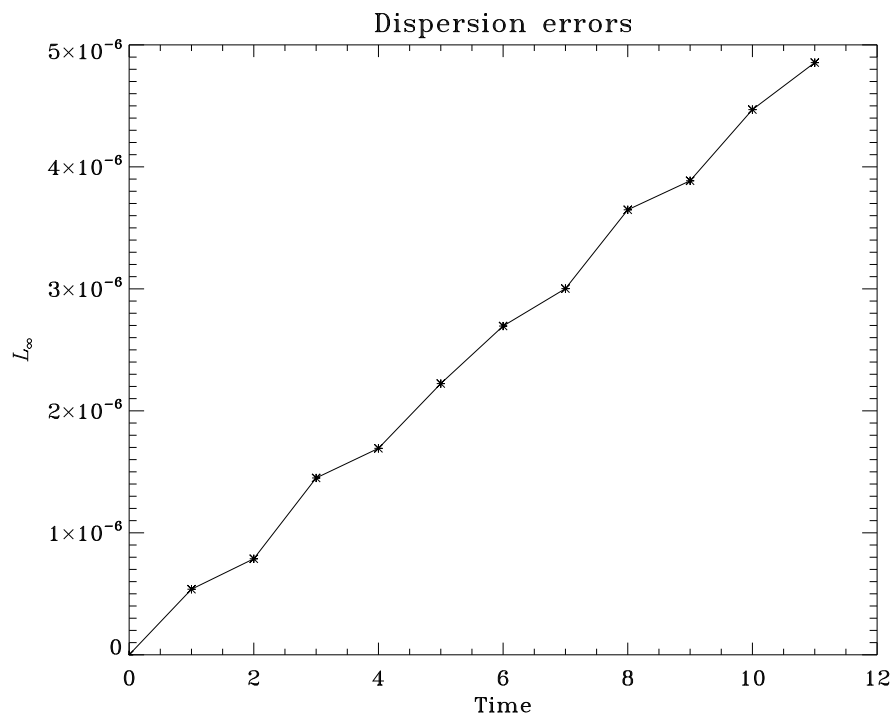


Figure 6: Dispersion errors measured as the L_∞ norm of $|v_z(x, y, z, t = n) - v_z(x, y, z, t = 0)|$, where $n = 0, 1 \dots 11$ for the $n_x = 32, n_y = 16 = n_z$ case.

free magnetic fields were very small $\sim 10^{-13}$.

Because the only non-divergence term in the energy equation (3) is the forcing term, upon integrating it over the volume, the divergence terms disappear and we recover:

$$\frac{\partial}{\partial t} \langle E \rangle = \int dV \rho \mathbf{v} \cdot \mathbf{F}, \quad (13)$$

where the term $\langle E \rangle$ is the volume integrated energy. We plot the simulated energy growth rate and the input forcing terms in panel (a) of Figure 7; although indistinguishable at the scale of the plot, there are differences between the two rates. It was established (not shown here), however, that the source of the discrepancies between the energy derivatives was almost entirely rooted in the time stepping scheme. Also of note is panel (d) of Figure 7; we estimate the differences between the temporal evolution profiles of the energies in the simulations with combined / only-FFT schemes. We define the energy as:

$$\text{error} = \frac{E_{\text{fft}} - E_{\text{comb}}}{E_{\text{fft}}} \times 100, \quad (14)$$

where E refers to either the kinetic or magnetic energies, and the subscripts denote the simulations with the different spatial schemes. The maximum error is of the order of 0.37%, probably due to the numerical damping of the high wave number modes by the compact finite differences. We show the spectrum of the Fourier modes in Figure 8. The spectra are almost indistinguishable in the two simulations in regions of wave numbers less than the de-aliasing limit. The magnetic and kinetic energies are seen to be very similar at the largest scales but start showing significant differences at higher wave numbers.

4. The ABC flow

As a final test case, we simulate the weakly compressible MHD free decay of Beltrami-type initial velocity and magnetic field conditions. We impose equipartition between the magnetic and kinetic energies at $t = 0$. Magnetic energy is thereafter enhanced by non-linear interactions, at the expense of the kinetic energy. To set the problem up, we choose a flow with $A_0 = 0.9, B_0 = 1, C_0 = 1.1$, and initial condition \mathbf{B} such that [e.g. 12]:

$$v_x = B_0 \cos(k_f y + \phi_{b,v}) + C_0 \sin(k_f z + \phi_{b,v}) = b_x, \quad (15)$$

$$v_y = C_0 \cos(k_f z + \phi_{b,v}) + A_0 \sin(k_f x + \phi_{b,v}) = b_y, \quad (16)$$

$$v_z = A_0 \cos(k_f x + \phi_{b,v}) + B_0 \sin(k_f y + \phi_{b,v}) = b_z, \quad (17)$$

where $0 \leq (x, y, z) < 2\pi$. The initial condition is chosen to be a combination of the modes $k_f = 2, 3$; $\phi_v \neq \phi_b$ are phases added to the initial conditions to avoid a completely Alfvénic initial condition. The viscosity and magnetic resistivity are set to $\mu = 0.0157 = \eta$. The number of grid points in the calculation is $n_x = 80 = n_y = n_z$ and the time step is $\Delta t = 10^{-4}$. We use the combined spatial scheme in order to compute the derivatives, i.e., FFTs along the horizontal

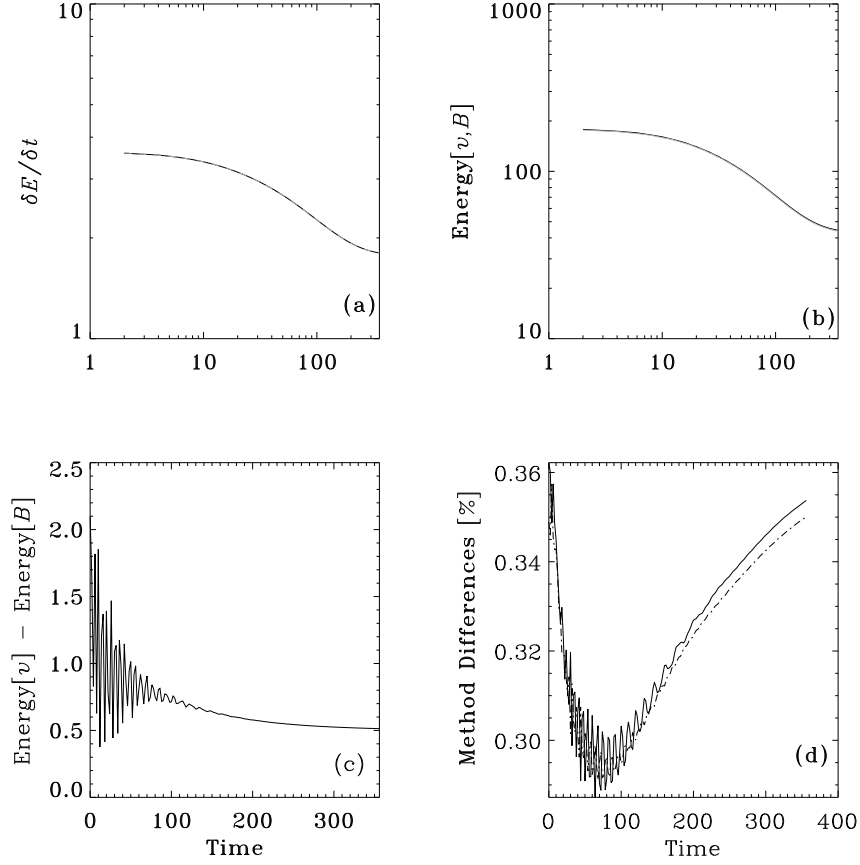


Figure 7: Results from simulations of a forced Archontis dynamo. Panel (a) shows the derivative of the total energy with the rate of energy input by the forcing term overplotted. The two are indistinguishable at this scale but it was seen (not shown here) that the dominant source of the differences was the accuracy of the time-stepping scheme. Panel (b) is a log-log plot of the temporal evolution of the magnetic and kinetic energies; they are also indistinguishable at this scale, a result not different from that established by [16]. The difference between the magnetic and kinetic energies is displayed in panel (c); the oscillations in the energy differences represent the creation and subsequent dissipation of small-scale Alfvén waves. Finally, panel (d) shows the difference in kinetic (dot-dash line) and magnetic (solid line) energies between the simulations with the all-FFT and combined schemes. The peak error, defined in equation (14), appears to occur right at the beginning, of the order of 0.36 %.

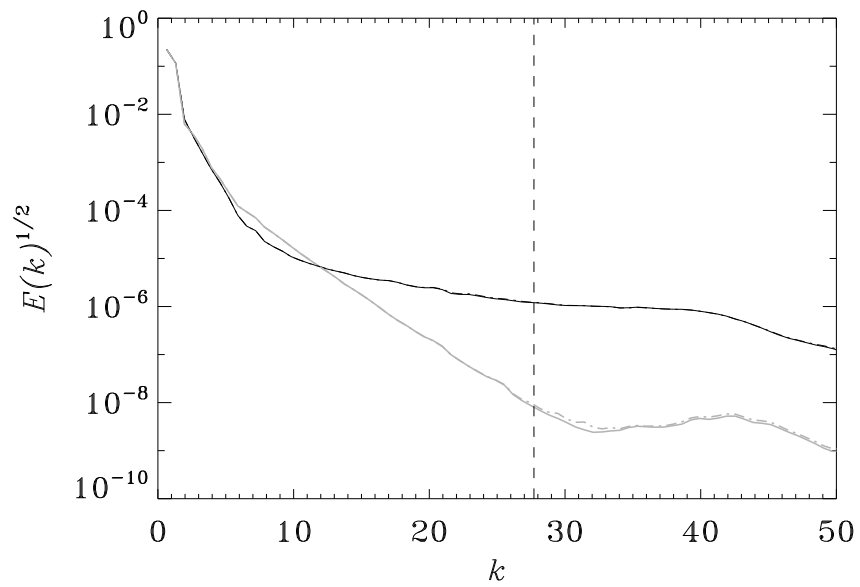


Figure 8: Spatial spectral distribution of the kinetic (thick lines) and magnetic (thin lines) energies at $t = 400$ from the Archontis dynamo simulation. The solid lines show the FFT scheme while the dot-dash lines denote the combined method. The vertical dashed line marks the location where the filter starts to damp the solution. At the large scales, the magnetic and kinetic energies show equipartition, and similar decay rates with spatial wave number. This is a consequence of $\mu = \eta$.

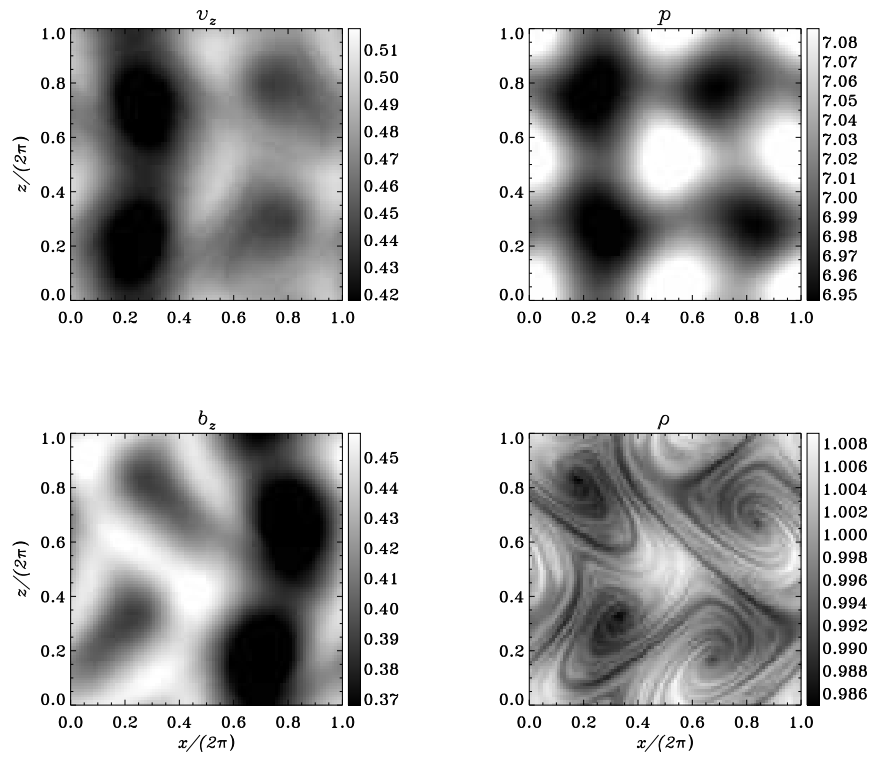


Figure 9: $x - z$ plane cuts of the variables at $t = 400$. The system has started to approach steady state. Scales for all except density have been saturated in order to enhance feature visibility.

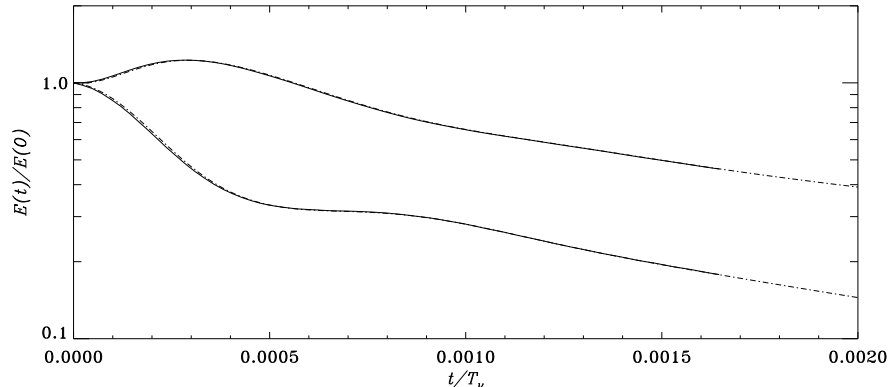


Figure 10: Time evolution of the magnetic (upper line) and kinetic (lower line) energies computed using two different codes (solid and dot-dash lines). The dot-dash lines are taken from an independent pseudo-spectral simulation of incompressible turbulence, computed using a code developed by [21]. The normalization term $T_\nu = (2\pi)^2/\mu$ is the diffusive time scale. The process of Alfvénization leads to the channeling of kinetic into magnetic energy. Essentially, the energy transfer results in the production of Alfvén waves; the fluid trips into a turbulent state within another diffusive timescale.

directions and compact finite differences along the z axis. In order to reduce the degree of compressibility, the initial pressure and density are chosen to be $p = 100$, $\rho = 1$ with $\gamma = 5/3$, meaning that the sound speed $c \sim 12.9$. The initial maximum Mach number of the flow is on the order of 0.1, implying that the situation is reflective of incompressible turbulence. We simulate the system in this limit because we wish to compare these results with an identical computation performed using an incompressible code developed independently by [21]. The time evolution of the kinetic and magnetic energies as computed by the two codes are displayed in Figure 10. The time on the horizontal axis of Figure 10 is normalized by the diffusive timescale, $T_\nu = (2\pi)^2/\mu = 2514.5$. The magnetic field passes through an initial growth period, caused by the Alfvénization process. Within a thousandth of a diffusive timescale, turbulence sets in and both the kinetic and magnetic energies decay rapidly. In Figure 11, we display the spatial scale distribution of the magnetic and kinetic energies. Over the entire temporal window of the simulation, we find $|\nabla \cdot \mathbf{B}| \lesssim 10^{-12}$, with a linear temporal error growth rate (see Figure 12).

The x, y, z directional spectra are shown in Figure 13. For example, to obtain the spectrum along the x direction (termed the k_x spectrum), we average the absolute value of the 3D Fourier transform of the magnetic energy over the $y-z$ plane. Differences between the three curves arise from the choice of initial conditions. We also comment on the diffusive properties of the scheme. We drop the resolution along the z direction and perform a simulation with the same initial conditions as that of the $n_x = 80 = n_y = n_z$ case. The directional spectra of the $n_z = 80, 60$ cases, shown in Figures 13 and 14, demonstrate that

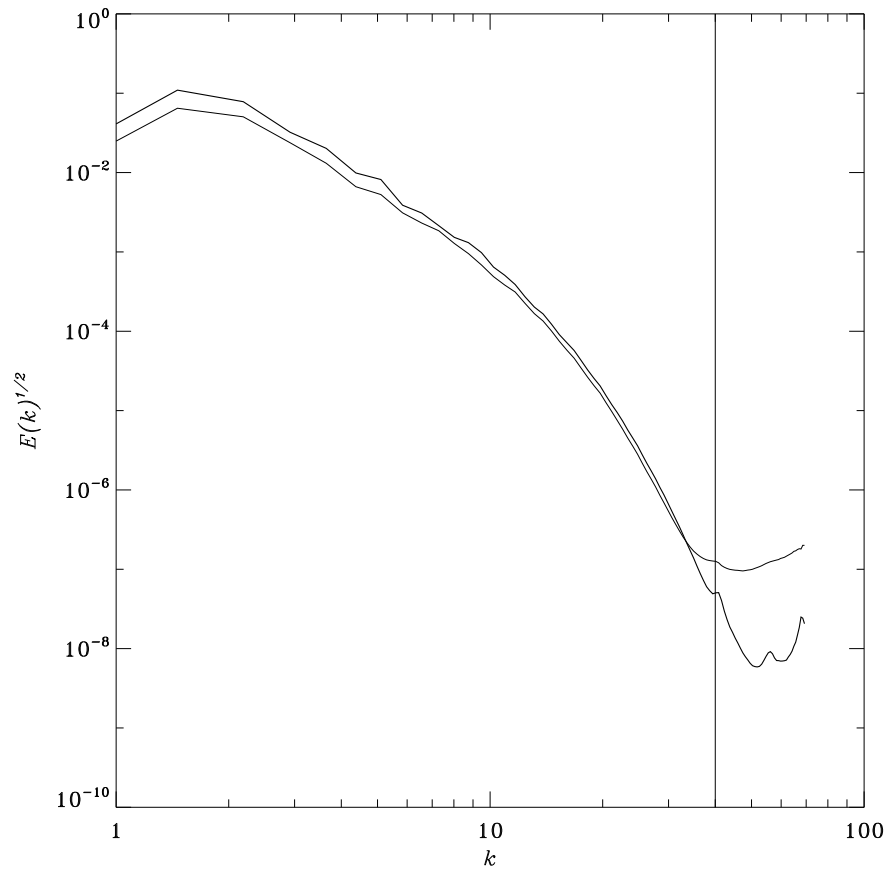


Figure 11: Spatial scales of the magnetic (thick line) and kinetic (thin line) energies at $t = 0.00117\tau_v$. The vertical line marks the spatial Nyquist.

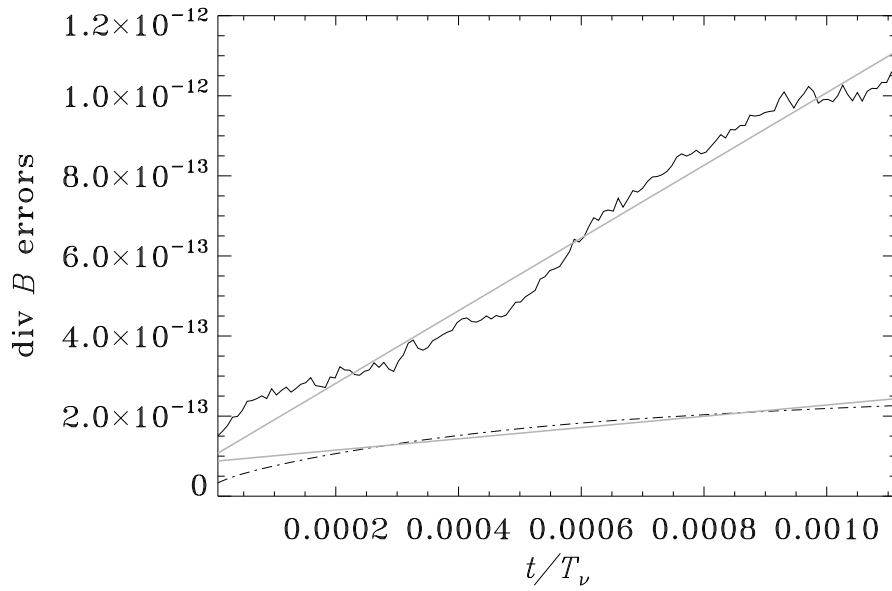


Figure 12: The time evolution of $(\max |\nabla \cdot \mathbf{B}|) / (\max |\mathbf{B}|)$ (solid dark line), the L_2 norm of $|\nabla \cdot \mathbf{B}|$ (dot-dash line) and linear fits to these two (thin lines). The growth rate of the error is linear in time, meaning that the error in the calculation can be safely contained over a large number of iterations. Since we use a non-staggered grid, the derivatives and values of the magnetic field components are defined numerically on the grid points.

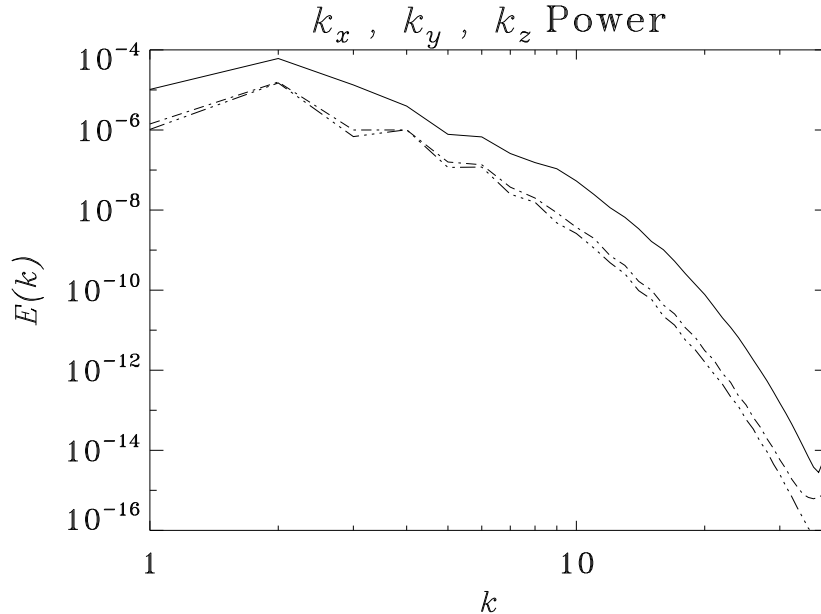


Figure 13: The magnetic energy power spectra along specific directions: solid line - x , double-dot dashed line - y , and dot-dashed line - z at $t = 0.0011T_\nu$. The differences in the power spectra of the initial conditions contribute to the difference in magnitudes between the three curves. In this calculation, $n_x = 80 = n_y = n_z$.

numerical diffusion is not significant at this resolution. With further reduction of resolution, the solution is significantly affected. This may be attributed to insufficient viscosity, leading to spectral blocking in the z direction, thereby strongly influencing the turbulence of the system as a whole. In other words, the diffusivity associated with the compact finite difference scheme is very low. Consequently, the calculation is sensitive to spectral blocking.

5. SUMMARY AND CONCLUSIONS

We have developed and validated a 3D non-linear compressible MHD solver. A fourth-order Runge-Kutta time integrator in conjunction with FFT and sixth-order accurate compact finite difference based spatial derivative schemes are implemented. The FFTs are used along spatial directions where periodic boundary conditions may be applied and the compact finite differences otherwise. Thus we anticipate applying a combined FFT + compact finite difference scheme when studying stratified plasmas, such as in the Sun.

The compact finite difference scheme was first tested on standard cases such as the 1D Sod hydrodynamic and Brio-Wu MHD shock tubes. The combined scheme was also tested on a rotated 3D version of the Sod tube. Note that

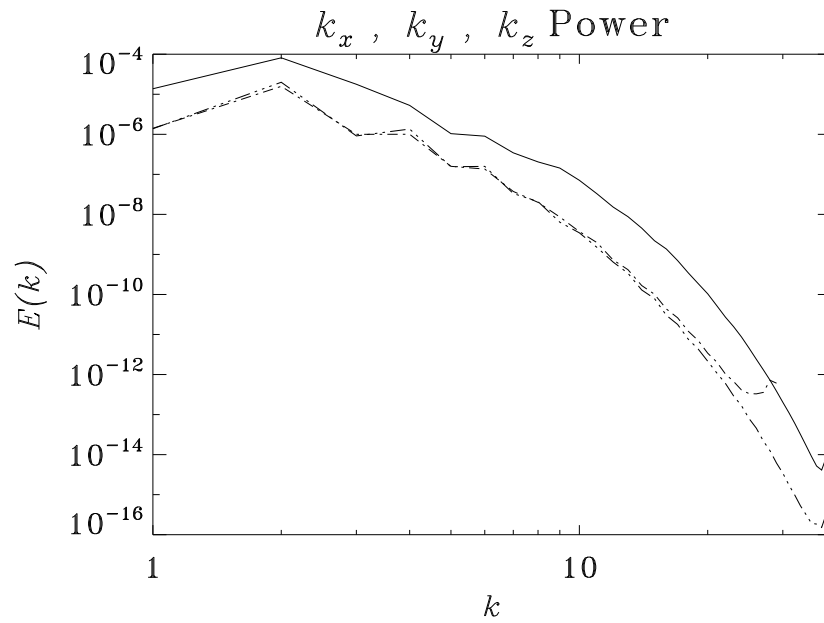


Figure 14: The magnetic energy power spectra along specific directions: solid line - x , double-dot dashed line - y , and dot-dashed line - z at $t = 0.0011T_L$. The differences in the power spectra of the initial conditions contribute to the difference in magnitudes between the three curves. In this calculation, $n_x = 80 = n_y, n_z = 60$. The similarities between the spectra in Figures 13 and this show that even with $n_z = 60$ points, the diffusive effects are not very important.

these tests were of a qualitative nature since low dissipation schemes such as compact finite differences are not ideally suited to capture shocks. In order to quantify the dispersion errors in the system, we simulated propagating circularly polarized Alfvén waves in two and three dimensions. In the two dimensional case, we used FFTs in both directions, and not surprisingly found the solutions to be very accurate. The wave was then rotated and 3D simulations with the two different spatial schemes were performed. There were small but detectable errors in the simulations with the combined scheme, errors that rapidly decreased with the system approaching convergence at higher resolutions. A Δx^{-6} error convergence rate was recovered.

We then proceeded to repeat results of previous studies of dynamos and MHD turbulence. In particular, we choose to simulate the isotropic cases of a forced compressible Archontis dynamo and free decay of an almost incompressible ABC flow. In the case of the Archontis dynamo, we performed the same computation with both the combined and all-FFT spatial schemes, and recovered practically indistinguishable spectra and energy growth rates. As for the free decay simulation, we compared the temporal evolution rates of the magnetic and kinetic energies with those extracted from an independent incompressible calculation of the same initial state [21]. The agreement was excellent. In all the calculations performed, the divergence of the magnetic field, measured either as the L_2 norm of $|\nabla \cdot \mathbf{B}|$ or as $(\max|\nabla \cdot \mathbf{B}|)/(\max|\mathbf{B}|)$, was always close to the numerical round-off error.

These calculations have lent us confidence in the numerical scheme and we believe the code to be sufficiently validated and verified. We find no evidence of strong numerical dissipation from employing compact finite differences in the z -direction. The dispersion effects of the scheme are also very small. With this solver, we plan on studying sub-grid scale models of MHD turbulence and the effect of stratification and rotation on inverse magnetic energy cascades. The non-linear aspects of the solver are only recent extensions to a pre-existing linear ideal-MHD wave code [9] developed to study wave propagation in the magnetic Sun; the tests herein will have also helped bolster the numerical basis of this original code.

6. Acknowledgements

All the simulations presented here were performed exclusively on the Stanford solar group machines. S.M.H. would like to extend warm regards towards P. Scherrer for having allowed this. We would also like to thank D. Rosenberg and R. Cameron for comments and suggestions. S.M.H. acknowledges funding from the German Aerospace Center (DLR) through grant FK Z 50 OL 0801 “German Data Center for SDO”.

References

- [1] F. Cattaneo, On the Origin of Magnetic Fields in the Quiet Photosphere, *Astrophysical Journal Letters* 515 (1999) L39–L42. doi:10.1086/311962.

- [2] U. Frisch, A. Pouquet, J. Lórat, A. Mazure, Possibility of an inverse cascade of magnetic helicity in magnetohydrodynamic turbulence, *Journal of Fluid Mechanics Digital Archive* 68 (04) (1975) 769–778. doi:10.1017/S002211207500122X.
- [3] A. Pouquet, U. Frisch, J. Lórat, Strong mhd helical turbulence and the nonlinear dynamo effect, *Journal of Fluid Mechanics Digital Archive* 77 (02) (1976) 321–354. doi:10.1017/S0022112076002140.
- [4] M. Meneguzzi, U. Frisch, A. Pouquet, Helical and nonhelical turbulent dynamos, *Phys. Rev. Lett.* 47 (15) (1981) 1060–1064. doi:10.1103/PhysRevLett.47.1060.
- [5] F. Cattaneo, D. W. Hughes, Dynamo action in a rotating convective layer, *Journal of Fluid Mechanics* 553 (-1) (2006) 401–418. doi:10.1017/S0022112006009165.
- [6] D. W. Hughes, F. Cattaneo, The alpha-effect in rotating convection: size matters, *Journal of Fluid Mechanics* 594 (-1) (2008) 445–461. doi:10.1017/S0022112007009214.
- [7] P. J. Käpylä, M. J. Korpi, A. Brandenburg, Large-scale dynamos in rigidly rotating turbulent convection, *ArXiv e-prints* arXiv:0812.3958.
- [8] S. M. Hanasoge, Theoretical studies of wave interactions in the sun, Ph.D. thesis, Stanford University (2007).
- [9] S. M. Hanasoge, Seismic Halos around Active Regions: A Magnetohydrodynamic Theory, *Astrophysical Journal* 680 (2008) 1457–1466. arXiv:0712.3578, doi:10.1086/587934.
- [10] S. M. Hanasoge, S. Couvidat, S. P. Rajaguru, A. C. Birch, Impact of locally suppressed wave sources on helioseismic traveltimes, *Monthly Notices of the Royal Astronomical Society* 391 (2008) 1931–1939. arXiv:0707.1369, doi:10.1111/j.1365-2966.2008.14013.x.
- [11] S. B. F. Dorch, V. Archontis, On the Saturation of Astrophysical Dynamos: Numerical Experiments with the No-Cosines Flow, *Solar Physics* 224 (2004) 171–178. arXiv:arXiv:astro-ph/0409193, doi:10.1007/s11207-005-5700-4.
- [12] V. Archontis, S. B. F. Dorch, Å. Nordlund, Dynamo action in turbulent flows, *Astronomy & Astrophysics* 410 (2003) 759–766. arXiv:arXiv:astro-ph/0306069, doi:10.1051/0004-6361:20031293.
- [13] A. Vögler, S. Shelyag, M. Schüssler, F. Cattaneo, T. Emonet, T. Linde, Simulations of magneto-convection in the solar photosphere. Equations, methods, and results of the MURaM code, *Astronomy & Astrophysics* 429 (2005) 335–351. doi:10.1051/0004-6361:20041507.

- [14] S. K. Lele, Compact finite difference schemes with spectral-like resolution, *Journal of Computational Physics* 103 (1) (1992) 16–42.
- [15] N. E. Hurlburt, A. M. Rucklidge, Development of structure in pores and sunspots: flows around axisymmetric magnetic flux tubes, *Monthly Notices of the Royal Astronomical Society* 314 (2000) 793–806.
- [16] R. Cameron, D. Galloway, Saturation properties of the Archontis dynamo, *Monthly Notices of the Royal Astronomical Society* 365 (2006) 735–746. doi:10.1111/j.1365-2966.2005.09749.x.
- [17] T. A. Gardiner, J. M. Stone, An unsplit godunov method for ideal mhd via constrained transport in three dimensions, *Journal of Computational Physics* 227 (8) (2008) 4123–4141.
- [18] M. Brio, C. C. Wu, An upwind differencing scheme for the equations of ideal magnetohydrodynamics, *Journal of Computational Physics* 75 (2) (1988) 400–422.
- [19] G. Tóth, The divb=0 constraint in shock-capturing magnetohydrodynamics codes, *Journal of Computational Physics* 161 (2) (2000) 605–652.
- [20] M. H. Carpenter, D. Gottlieb, S. Abarbanel, The stability of numerical boundary treatments for compact high-order finite-difference schemes, *Journal of Computational Physics* 108 (2) (1993) 272 – 295. doi:DOI: 10.1006/jcph.1993.1182.
- [21] D. O. Gómez, P. D. Mininni, P. Dmitruk, Mhd simulations and astrophysical applications, *Advances in Space Research* 35 (5) (2005) 899–907.